


 Cite this: *Chem. Commun.*, 2025, 61, 2297

 Received 21st November 2024,
 Accepted 4th January 2025

DOI: 10.1039/d4cc06188h

rsc.li/chemcomm

Phosphorus-doped nickel–iron hydroxides/MXene for efficient electrochemical water oxidation†

 Ya Cao,^{‡,a} Jiangchuan Liu,^{‡,a} Siqi Xu,^a Yunjiao Yang,^a Yi Yu,^{id} *^c Zhidong Chen^{id} *^b and Changhai Liu^{id} *^a

Herein, NiFeP/Ti₂C@NF was synthesized from a hydrothermal process and chemical conversion, and exhibited a low overpotential of 177 mV at $j = 50 \text{ mA cm}^{-2}$, a low Tafel slope of 56 mV dec^{-1} , and a very competitive stable activity in alkaline electrolyte, proposing a strategy for efficient OER and overall water splitting.

The electrochemical water decomposition process comprises two key reactions: the hydrogen evolution reaction (HER) and the oxygen evolution reaction (OER). The OER represents a rate-determining step for total water decomposition due to its kinetic retardation and poor energy conversion efficiency, which involves a coupled four-electron-proton transfer.¹ Therefore, the development of a low-cost, efficient, energy-efficient, and long-lasting non-precious-metal catalyst is crucial to enhance the slow kinetics of the OER. Currently, mainly noble metal catalysts, such as RuO₂, are employed for the OER under alkaline conditions. However, their high cost and scarcity restrict their large-scale practical applications. Consequently, there is a pressing need to identify alternative OER catalysts to those derived from noble metals.^{2–4} Layered double hydroxides (LDHs) represent highly efficient electrocatalysts for the OER due to their unique layered structure, modifiable interlayer anions, favorable oxygen evolution pathway, and synergistic effect between the metal hydroxide layers and interlayer anions. Among these materials, NiFe LDHs exhibit excellent OER electrocatalytic activity due to the synergistic interaction between Ni and Fe and their tunable electronic structures. However, the weaker electron transfer ability of NiFe LDHs leads to a reduction in catalytic activity. To address

this issue, the catalytic properties of LDHs can be effectively modulated by introducing heteroatoms, such as phosphides and sulfides, to enhance their intrinsic activities.^{5–7}

Nevertheless, LDHs are susceptible to agglomeration, which also impairs their performance in the OER. One common approach to addressing this issue is to grow LDHs *in situ* on conductive carriers, such as MXene, graphene, carbon nanotubes, nickel foam, and so forth. MXene's tunable metal element composition, which ensures the high electrical conductivity of the MXene material, enhances the electronic conductivity, activity, and stability of the catalytic process. Additionally, MXene's surface functional groups facilitate the adsorption of reactants in the electrocatalytic process.^{8–10} In view of the above excellent properties of MXene, MXene serves not only as an anchoring site for the highly dispersed nanostructured active phases, but also as an excellent conductive substrate, which enhances the hybrids' charge transfer kinetics.

In this study, the NiFeP/Ti₂C@NF catalysts were designed and synthesized by *in situ* growing phosphated NiFe LDH on Ti₂C MXene-loaded nickel foam using a hydrothermal and calcined phosphatization method after NaBH₄ treatment (Fig. 1a). With regard to the preparation of phosphides, NaBH₄ reduction is often employed in order to promote the effect of the phosphatisation reaction. This involves the removal of some of the oxygen atoms in the samples and the creation of defects, with the intention of improving the phosphatisation effect. This approach was taken in order to exploit the synergistic effect of MXene and phosphated LDH. The vertically interspersed nano-arrays synthesised by this method exhibited a large specific surface area.

Powder X-ray diffraction (XRD) is a powerful tool for characterizing Ti₂AlC phases and Ti₂C MXene as shown in Fig. 1b. It can be observed that during the exfoliation process, the diffraction peaks of Ti₂AlC disappeared and the (002) peak was kept at a lower angle. After acid etching, the most intense peak for Ti₂C is typically the (002) at $2\theta = 7.6^\circ$ reflection, due to the *c*-axis of the hexagonal lattice, suggesting the successful synthesis of MXene. The *d* for the basal plane of Ti₂C is $\sim 2.32 \text{ nm}$ calculated from Bragg's equation.^{11,12} In the case of the NiFe/Ti₂C@NF sample in Fig. 1c, the peaks are clearly

^a School of Materials Science and Engineering, CNPC-CZU Innovation Alliance, Key Laboratory of Materials Surface Science and Technology of Jiangsu Province Higher Education Institutes, Changzhou University, Changzhou, 213164, Jiangsu, China. E-mail: liuch@cczu.edu.cn

^b School of Petrochemical Engineering, Changzhou University, Changzhou, 213164, Jiangsu, China. E-mail: zdchen@cczu.edu.cn

^c Center for Transformative Science, ShanghaiTech University, Shanghai, 201210, China. E-mail: yuyi2@shanghaitech.edu.cn

† Electronic supplementary information (ESI) available. See DOI: <https://doi.org/10.1039/d4cc06188h>

‡ These authors (Ya Cao and Jiangchuan Liu) contributed equally to this work.

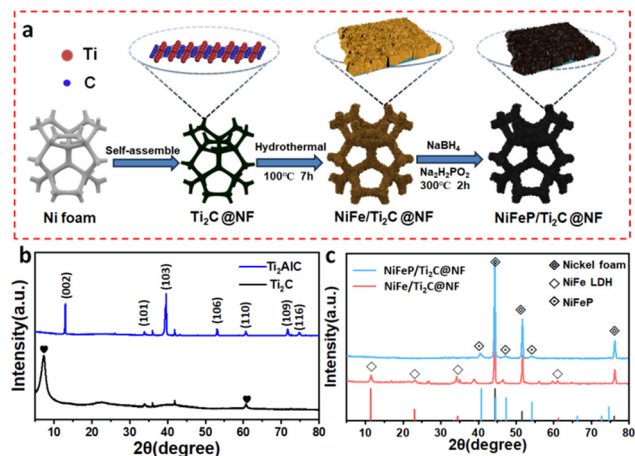


Fig. 1 (a) Schematic diagram of the synthesis process, XRD patterns of (b) Ti_2AlC and Ti_2C , and (c) $\text{NiFeP}/\text{Ti}_2\text{C}@/\text{NF}$ and $\text{NiFe}/\text{Ti}_2\text{C}@/\text{NF}$ samples.

visible at 11.41° , 22.974° , 33.536° , 34.425° , 38.992° , 45.985° , 59.938° , and 61.254° , which correspond to (003), (006), (006), (106), and (106), respectively, for the NiFe LDH (JCPDS no. 40-0215) crystal plane.¹² However, after the NaBH_4 treatment and phosphorization process, no signals of NiFe LDH were observed in $\text{NiFeP}/\text{Ti}_2\text{C}@/\text{NF}$, suggesting the successful synthesis of NiFeP species. The morphology of the samples was also characterised, as illustrated in Fig. S1 (ESI[†]). This figure demonstrates that the flaky Ti_2C MXene was uniformly and densely adhered to the bare NF substrate following soaking in CTAB and MXene dispersions. This also corroborates the synthesis of the single oligolayer of Ti_2C and the successful preparation of the $\text{Ti}_2\text{C}@/\text{NF}$ substrate.

Fig. 2a and b illustrate the surface morphology of the $\text{NiFe}/\text{Ti}_2\text{C}@/\text{NF}$ and $\text{NiFeP}/\text{Ti}_2\text{C}@/\text{NF}$ samples. Compared with the morphology of the samples prior to phosphatisation, the scale of the nanosheets is increased, the distribution of nanosheets is more dense, and the overall distribution of the nanosheets becomes homogeneous as a result of stacking (Fig. S1, ESI[†]). The convoluted Ti_2C can efficiently promote the deposition of NiFe LDH, improving the contact area with the electrolyte and the specific surface area of the reaction. The $\text{NiFeP}/\text{Ti}_2\text{C}@/\text{NF}$ sample was then subjected to further characterisation by TEM (Fig. 2c–f). The surface of the Ti_2C nanosheet is observed to contain a considerable number of minute NiFeP nanoparticles (NPs), which manifest the presence of lattice diffraction fringes with spacings of 0.221 nm and 0.203 nm, respectively. These spacings correspond to the (111) and (201) crystalline facets of NiFeP NPs. Furthermore, the homogeneous distribution of the elements Ti, C, Ni, Fe and P in the elemental mapping confirmed the successful synthesis of P–NiFe/ $\text{Ti}_2\text{C}@/\text{NF}$.

In order to investigate the valence states of the elements present in the catalysts, the samples were analysed using X-ray photoelectron spectroscopy (XPS) and the full spectra of the samples are displayed in Fig. S2 (ESI[†]), confirming the presence of P element in $\text{NiFeP}/\text{Ti}_2\text{C}@/\text{NF}$. Fig. S3a (ESI[†]) illustrates the typical satellite peaks of Ni in the NiFe LDH sample at 879.5 and 861.6 eV, as well as the characteristic peaks at 856.0 and 873.4 eV, which can be attributed to $\text{Ni}^{2+} 2p_{3/2}$ as well as $\text{Ni}^{2+} 2p_{1/2}$. With the NaBH_4 treatment and phosphorylation process, the typical peak of Ni^0 species at

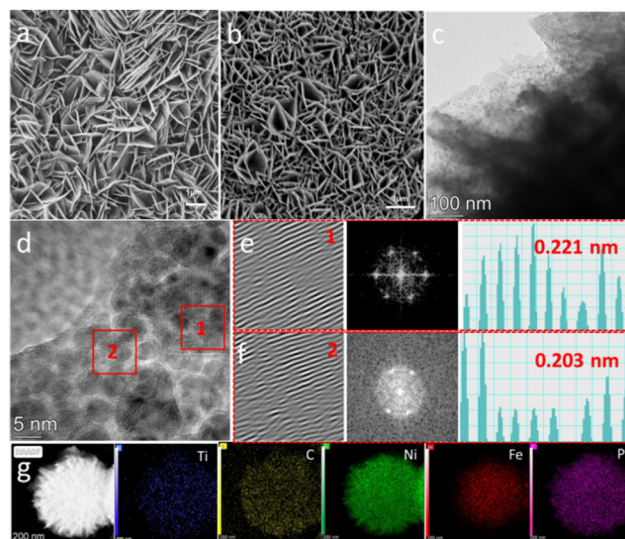


Fig. 2 SEM images of (a) $\text{NiFe}/\text{Ti}_2\text{C}@/\text{NF}$ and (b) $\text{NiFeP}/\text{Ti}_2\text{C}@/\text{NF}$. (c)–(f) TEM images and (g) elemental mapping of $\text{NiFeP}/\text{Ti}_2\text{C}@/\text{NF}$.

approximately 853.4 eV can be found in the sample of $\text{NiFeP}@/\text{NF}$ and $\text{NiFeP}/\text{Ti}_2\text{C}@/\text{NF}$, indicating the reduction of NiFe LDH and oxygen extraction during the process.¹³ Likewise, Fe^0 species at approximately 750.7 eV also appear in the sample of $\text{NiFeP}@/\text{NF}$ and $\text{NiFeP}/\text{Ti}_2\text{C}@/\text{NF}$ compared to the sample of NiFe LDH@NF (Fig. 3b). The appearance of Ni^0 over Fe^0 peaks provides evidence that the phosphated samples were successfully prepared, which is consistent with the XRD and TEM results. The peaks of the $\text{NiFeP}/\text{Ti}_2\text{C}@/\text{NF}$ samples prepared on the MXene substrate exhibited a change in their characteristics. The change in position may be attributed to reduction treatment and the spontaneous transfer of electrons from Ni and Fe to the MXene substrate in the composite structure consisting of NiFe LDH and Ti_2C MXene. In addition, the characteristic peak appears at 129 eV. The P 2p XPS data are illustrated in Fig. S3c (ESI[†]), testifying the successful introduction of P in NiFe LDH. Due to the electronegative P sites as a proton acceptor, the electronic structures of Ni and Fe accelerate the charge transfer.

In order to evaluate the electrochemical performance of the samples, commercial RuO_2 loaded on NF was selected for comparison. The $\text{RuO}_2@/\text{NF}$ sample was tested in conjunction with the precursors $\text{NiFe}@/\text{NF}$, $\text{NiFe}/\text{Ti}_2\text{C}@/\text{NF}$, and $\text{NiFeP}@/\text{NF}$, as well as bare NF, which served as the comparative catalysts. The OER electrocatalytic performance of this nanosheet structure was evaluated using a standard three-electrode system in 1 M KOH solution. The potential range was 0–1.6 V vs. RHE at a scan rate of 5 mV s^{-1} . The linear scanning voltammetry (LSV) curves illustrated in Fig. 3a obtained from the tests indicate that the $\text{NiFeP}/\text{Ti}_2\text{C}@/\text{NF}$ sample can reach a current density of 50 mA cm^{-2} at an extremely low overpotential of 177 mV (1.407 V with respect to the reversible hydrogen electrode), which is smaller than the overpotentials of the $\text{NiFe}@/\text{NF}$ (267 mV), $\text{NiFe}-\text{Ti}_2\text{C}@/\text{NF}$ (281 mV), $\text{NiFeP}@/\text{NF}$ (247 mV), $\text{RuO}_2@/\text{NF}$ (383 mV), NF (408 mV), respectively. The test results demonstrate that the $\text{NiFeP}/\text{Ti}_2\text{C}@/\text{NF}$ samples, which exhibit uniform vertical interlacing of nanosheets, exhibit a more favourable

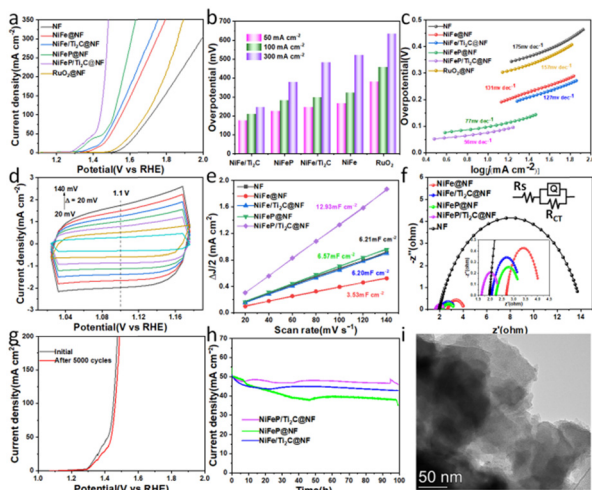


Fig. 3 (a) LSV, (b) comparison of overpotentials at different current densities, (c) Tafel plots, (d) CV at different scan rates, (e) C_{dl} and (f) Nyquist plots for different electrocatalysts. (g) Cycling stability after 5000 cycles of NiFeP/Ti₂C@NF. (h) Chronopotentiometry curves of different catalysts and (i) morphology after long-term measurement of NiFeP/Ti₂C@NF.

OER catalytic performance compared to the other comparison samples. Furthermore, the samples exhibited a comparable trend at a current density of 100 and 300 mA cm⁻² in Fig. 3b. The reaction kinetics of all the samples were evaluated through a comparative analysis of the Tafel slopes obtained from regional linear fitting. As displayed in Fig. 3c, it can be observed that the NiFeP/Ti₂C@NF sample exhibits the lowest Tafel slope of 56 mV dec⁻¹, which is less than that of comparison samples, indicating the high reaction kinetics and good OER catalytic performance with phosphorization and Ti₂C introduction, which is consistent with the LSV test results. Moreover, the electrochemically active surface area (ECSA) of the catalyst is proportional to the electrochemical double layer capacitance (C_{dl}).^{14,15} Consequently, the electrochemical double layer capacitance was evaluated through the measurement of cyclic voltammetry (CV) curves in the non-Faraday region of the sample, employing different scan rates (Fig. 3d and Fig. S4, ESI[†]). As illustrated in Fig. 3e, the C_{dl} value of the NiFeP/Ti₂C@NF sample, following the test fitting, is 12.93 mF cm⁻², which is considerably larger than that of NF (6.21 mF cm⁻²), NiFe@NF (3.53 mF cm⁻²), NiFe/Ti₂C@NF (6.20 mF cm⁻²) and NiFeP@NF (6.20 mF cm⁻²). The electrochemical active area and the number of electrocatalytic active sites were found to be larger for the vertically interleaved nanosheet-like, uniformly arranged NiFeP/Ti₂C catalysts, which were grown with MXene loaded on nickel foam as the substrate. This resulted in an enhanced performance with regard to the OER.

The electrochemical impedance spectroscopy (EIS) was evaluated within a frequency range of 100 kHz to 0.01 Hz, employing an alternating current perturbation of 10 mV. A simplified equivalent circuit was employed for the fitting of the EIS data. The Nyquist curves and the fitted equivalent circuit model are presented in Fig. 3f and Table S1 (ESI[†]). R_s and R_{CT} are understood to correspond to the solution impedance and charge transfer impedance, respectively. The NiFeP/Ti₂C@NF exhibits the smallest radius and R_{CT} relative to the other electrocatalysts, suggesting that the loading of the MXene

substrate reduces the resistance of the catalysts and enhances the charge transfer rate at the electrode–electrolyte interface. In order to gain a deeper understanding of the reaction kinetics during the oxygenation process, *in situ* EIS measurements were carried out, and the bode phase diagrams of the samples at different potentials were plotted. The bode phase diagrams of NiFeP/Ti₂C@NF can be divided into two distinct regions: the high-frequency region (102–103 Hz) and the low-frequency region (0.1–101 Hz). The high-frequency region is associated with the capacitance of the catalyst surface bilayer, whereas the low-frequency region is linked to the non-uniform charge distribution resulting from the OER. The onset potential for the oxygen evolution reaction (OER) for NiFeP@NF is 1.6 volts relative to the reversible hydrogen electrode (RHE), as illustrated in Fig. S5a (ESI[†]).^{16,17} The onset of the OER peaks following the loading of the sample NiFeP/Ti₂C@NF on the MXene substrate occurs at 1.5 V (*vs.* RHE), with a potential decrease of 100 mV in Fig. S5b (ESI[†]). This result is consistent with those obtained by LSV, thereby providing further evidence that the MXene substrate accelerates the electron transfer rate at the interface.

The electrochemical stability of the samples was evaluated using continuous CV scanning, current step and current-time curves (*i-t*) for the NiFeP/Ti₂C@NF sample, as this property is crucial for measuring the electrochemical performance of the catalysts. As illustrated in Fig. 3g, the sample overpotential exhibited an increase from 177 mV@50 mA cm⁻² to 191 mV@50 cm⁻² following 5000 turns of CV cycling, while maintaining 92% stability. As illustrated in Fig. S6 (ESI[†]), the current density exhibited a response at 50–250 mA cm⁻² and remained stable at each current density for one hour. Following a 100 hour period, when the current density was restored to 50 mA cm⁻², the potential remained stable with minimal fluctuation, indicating that the NiFeP/Ti₂C@NF has good durability. Fig. 3h presents *i-t* curves for the comparison samples, which demonstrates that the current density remained relatively stable with minimal decay after long-term electrolysis at 50 mA cm⁻² for 100 h. This confirms the electrocatalytic durability of NiFeP/Ti₂C@NF. Moreover, the samples subjected to the stability test were characterised morphologically. The SEM images demonstrated that the original, neatly arranged nanosheet arrays of NiFeP/Ti₂C@NF underwent a transformation after the OER stability test, exhibiting a convoluted structure. The entire structure was observed to be arranged in a petal-like configuration. The macroscopic morphology indicated that the structural collapse resulting from the generation of bubbles led to a certain reduction in performance. The macroscopic morphology indicates that the structure collapses as a result of the generation of bubbles, which in turn leads to a reduction in performance.

In order to evaluate the overall hydrolysis performance of the samples, a two-electrode electrolyzer comprising both the anode and cathode, namely NiFeP/Ti₂C@NF, was constructed in a 1 M KOH solution. Fig. 4a illustrates the LSV of the total desolvation water of NiFeP/Ti₂C@NF and a comparison sample in 1 M KOH electrolyte. The lowest total desolvation water overpotential was observed for NiFeP/Ti₂C@NF, at a current density of 10 mA cm⁻², with a value of 1.59 V. Fig. 4b illustrates the chronoamperometric current curves for the total desolvation water of the sample NiFeP/Ti₂C@NF and its comparison

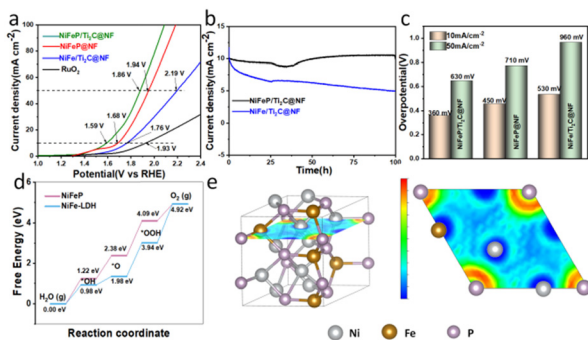


Fig. 4 (a) Polarization, (b) chronopotentiometry curves and (c) comparison of overpotentials for overall water splitting catalysis, (d) free energy diagram of the OER at $U = 0$ V in NiFeP and NiFe-LDH and (e) the ELF of NiFeP at the (001) surface.

samples. The results demonstrate that the NiFeP/Ti₂C@NF overpotential exhibits a lower attenuation in the 100 h total solution water stability test, and its stability is superior to that of the other comparison samples (Fig. 4c).

The Gibbs free energies of the OER intermediates of the NiFeP and NiFe-LDH were calculated in order to evaluate the reaction thermodynamics. In general, the step with the largest Gibbs energy barrier is considered to be the rate-determining step.^{18,19} As illustrated in Fig. 4d, the most significant barrier to the OER is observed in the transformation of [O*] to [*OOH] in both NiFeP and NiFe-LDH, with an energy barrier of 1.71 eV and 1.96 eV, respectively. It can be posited that NiFeP will exhibit superior OER performance in comparison to NiFe-LDH. Furthermore, the total density of states (TDOS) and projected density of states (PDOS) for NiFeP are presented in Fig. S7 (ESI[†]). It is evident that the absence of a band gap in NiFeP is indicative of its superior conductivity. Furthermore, the 3d orbitals of Ni and Fe form π backbonding with the 3d or 4d orbitals of P. The 3d orbitals of Ni and Fe form bonding orbitals with decreasing energy, while the 3d or 4d orbitals of P form antibonding orbitals with increasing energy. Consequently, the 3d orbitals of Ni and Fe are predominantly situated below the Fermi energy level, whereas the electronic orbital of P is primarily located above this level. It is notable that the PDOS of Ni, Fe, and P exhibit analogous peak shapes at analogous positions, thereby substantiating the existence of robust electronic interactions between the disparate elements. This is further corroborated by the ELF (Fig. 4e), which demonstrates that the electrons surrounding the Ni and Fe atoms exhibit pronounced off-domain characteristics and exert a significant influence on the electrons in the vicinity of P. The PDOS of NiFeP serves as an illustrative example of this phenomenon. The strong electronic interactions may permit NiFeP to exhibit enhanced reaction rates and kinetic properties in the OER reaction.

The resulting NiFeP/Ti₂C@NF exhibited a low overpotential of 177 mV and a low Tafel slope of 56 mV dec⁻¹ at 50 mA cm⁻² in the electrolyte of 1 M KOH. The addition of MXene prevented the agglomeration of phosphorylated LDH and enhanced the

electrical conductivity of the catalysts, thereby providing a greater number of reactive sites in comparison to the control sample. This study proposes a favourable solution for the design of high-performance MXene-loaded NiFe-based OER catalysts, which addresses the issues of low conductivity and the tendency for the original NiFe LDH to agglomerate.

This work was supported by the National Key Research and Development Program of China (2021YFB3502000), the Sponsored by Shanghai Rising-Star Program (21QA1406200), the National Natural Science Foundation of China (22072093, 22178031), Jiangsu Province Engineering Research Center of Intelligent Manufacturing Technology for the New Energy Vehicle Power Battery, Major Natural Science Research Projects of Universities in Jiangsu Province (21KJ4480001), and Changzhou Leading Innovative Talents Introduction and Cultivation (CQ20230108).

Data availability

The data supporting this article have been included as part of the ESI.[†]

Conflicts of interest

There are no conflicts to declare.

Notes and references

- H. Li, Y. Lin, J. Duan, Q. Wen, Y. Liu and T. Zhai, *Chem. Soc. Rev.*, 2024, **53**, 10709–10740.
- H. Over, *ACS Catal.*, 2021, **11**, 8848–8871.
- K. Du, L. Zhang, J. Shan, J. Guo, J. Mao, C. C. Yang, C. H. Wang, Z. Hu and T. Ling, *Nat. Commun.*, 2022, **13**, 5448.
- H. Sun, J. M. Yang, J. G. Li, Z. Li, X. Ao, Y. Z. Liu, Y. Zhang, Y. Li, C. Wang and J. Tang, *Appl. Catal., B*, 2020, **272**, 118988.
- R. Gao, J. Zhu and D. Yan, *Nanoscale*, 2021, **13**, 13593–13603.
- N. S. Gultom, H. Abdullah, C. N. Hsu and D. H. Kuo, *Chem. Eng. J.*, 2021, **419**, 129608.
- B. Singh, O. Prakash, P. Maiti, P. W. Menezes and A. Indra, *Chem. Commun.*, 2020, **56**, 15036–15039.
- M. Li, R. Sun, Y. Li, J. Jiang, W. Xu, H. Cong and S. Han, *Chem. Eng. J.*, 2022, **431**, 133941.
- B. Shen, Y. Feng, Y. Wang, P. Sun, L. Yang, Q. Jiang, H. He and H. Huang, *Carbon*, 2023, **212**, 118141.
- B. R. Anne, J. Kundu, M. K. Kabiraj, J. Kin, D. Cho and S. I. Choi, *Adv. Funct. Mater.*, 2023, **33**, 2306100.
- S. Aydinyan, *Ceram. Int.*, 2024, **50**, 12263–12269.
- D. Liu, Y. Yang, J. Zhang, L. Wang, Z. Ma, L. Ren, J. Wang, B. Xue and F. Li, *J. Alloys Compd.*, 2023, **941**, 168994.
- D. Tyndall, M. J. Craig, L. Gannon, C. McGuinness, N. McEvoy, A. Roy, M. Garcia-Melchor, M. P. rowne and V. Nicolosi, *J. Mater. Chem. A*, 2023, **11**, 4067–4077.
- F. Dionigi, J. Zhu, Z. Zeng, T. Merzdorf, H. Sarodnik, M. Gliech, L. Pan, W. X. Li, J. Greeley and P. Strasser, *Angew. Chem.*, 2021, **133**, 14567–14578.
- S. S. Jeon, P. W. Kang, M. Klingenhof, H. Lee, F. Dionigi and P. Strasser, *ACS Catal.*, 2023, **13**, 1186–1196.
- R. Suarez-Hernandez, G. Ramos-Sánchez, M. A. Oliver-Tolentino and I. González, *Electrochim. Acta*, 2021, **397**, 139240.
- A. R. Burton, R. Paudel, B. Matthews, M. Sassi, S. R. Spurgeon, B. H. Farnum and R. B. Comes, *J. Mater. Chem. A*, 2022, **10**, 1909–1918.
- G. Lippert, J. Hutter and M. Parrinello, *Mol. Phys.*, 1997, **92**, 477–487.
- C. Hartwigsen, S. Goedecker and J. Hutter, *Phys. Rev. B: Condens. Matter Mater. Phys.*, 1998, **58**, 3641–3662.